

Modelling of the Evolving Stable Boundary Layer

Zbigniew Sorbjan

Received: 19 July 2013 / Accepted: 4 December 2013 / Published online: 28 December 2013
© The Author(s) 2013. This article is published with open access at Springerlink.com

Abstract A single-column model of the evolving stable boundary layer (SBL) is tested for self-similar properties of the flow and effects of ambient forcing. The turbulence closure of the model is diagnostic, based on the K-theory approach, with a semi-empirical form of the mixing length, and empirical stability functions of the Richardson number. The model results, expressed in terms of local similarity scales, are universal functions, satisfied in the entire SBL. Based on similarity expression, a realizability condition is derived for the minimum allowable turbulent heat flux in the SBL. Numerical experiments show that the development of “horse-shoe” shaped, fixed-elevation hodographs in the interior of the SBL around sunrise is controlled by effects imposed by surface thermal forcing.

Keywords Gradient-based similarity · Heat-flux realizability condition · Inertial oscillations · Single-column model · Stable boundary layer

1 Introduction

Significant interest in the structure and properties of the stable boundary layer (SBL), observed during recent years, resulted in a number of field programs (e.g., Cuxart et al. 2000; Kustas et al. 2004; Schwarz et al. 2004; Oncley et al. 2007; Thomas et al. 2008), major field experiments, such as SHEBA (e.g., Andreas et al. 1999; Persson et al. 2002; Grachev et al. 2005), and CASES-99 (e.g. Blumen et al. 2001; Poulos et al. 2002), as well as numerical model intercomparisons (e.g., Beare et al. 2006; Cuxart et al. 2006) and investigations (e.g., Sun et al. 2006; Sanz Rodrigo and Anderson 2013). The field observations showed that an ample understanding of the stably stratified boundary layer depends on high-resolution vertical measurements. Instantaneous turbulent flows in stable conditions contain thin layers with large, positive and negative vertical gradients of the potential temperature and

Z. Sorbjan (✉)
Department of Physics, Marquette University, Milwaukee, WI 53201-1881, USA
e-mail: zbigniew.sorbjan@mu.edu

Z. Sorbjan
Institute of Geophysics, Polish Academy of Sciences, Warsaw, Poland

wind velocity (e.g., Sorbjan and Balsley 2008). The SBL often does not reach equilibrium (e.g., Sun et al. 2004), is sensitive to terrain inclination, which can lead to the development of a variety of density currents (e.g., Derbyshire and Wood 1994; Monti et al. 2002) and shallow drainage flows (e.g., Mahrt et al. 2001; Shapiro and Fedorovich 2009). It is often affected by baroclinicity (Kim and Mahrt 1992), subsidence (Mirocha and Kosovich 2010), surface heterogeneity (e.g., Nappo 1991), and radiative effects (e.g., Duynkerke 1999; Sun et al. 2003; Ha and Mahrt 2003).

Despite the described complications, numerical studies, involving both large-eddy simulation (LES) and single-column models (SCM), produce reasonable results in weakly stable conditions (Kosovic and Curry 2000; Beare et al. 2006; Stoll and Porté-Agel 2008). Thus, the primary purpose of this study is to further investigate properties of the SCM approach as a key to the understanding of nocturnal turbulence. Specifically, we focus on the consistency of turbulence parametrization, self-similar properties of the flow, and the effects of ambient forcing.

The paper has the following structure: model equations and assumptions are discussed in Sect. 2 and model results are compared with large-eddy simulations in Sect. 3. In the same section, the universal functions of the Richardson number are derived based on the turbulence closure equations. The effects of the surface forcing are discussed in Sect. 4, and final remarks are provided in Sect. 5.

2 Model

2.1 Governing Equations

The presented model is an improved version of the single-column model (SCM) developed by Sorbjan (2012b). It employs the ensemble-averaged, horizontally-homogeneous equations for the wind components and temperature in the atmospheric boundary layer of the form,

$$\frac{\partial U}{\partial t} = f(V - V_g) - \frac{\partial \tau_x}{\partial z} + s_u, \quad (1a)$$

$$\frac{\partial V}{\partial t} = -f(U - U_g) - \frac{\partial \tau_y}{\partial z} + s_v, \quad (1b)$$

$$\frac{\partial \Theta}{\partial t} = -\frac{\partial H}{\partial z} + s_\theta, \quad (1c)$$

where U , V are the horizontal components of the wind vector, U_g , V_g are the components of the geostrophic wind, f is the Coriolis parameter, Θ is the potential virtual temperature, τ_x , τ_y , and H are the turbulent fluxes for momentum and temperature, z is the height, and t is time. The first two equations of the system above are the momentum budgets, and the third equation follows from the budget of the virtual potential temperature. The terms s_u , s_v , and s_θ express the effects of external forcing (which can include the effects of baroclinicity, radiation, subsidence, etc.).

The turbulent fluxes in Eq. 1 are evaluated based on K-theory (Prandtl 1932),

$$\tau_x = -K_m \frac{dU}{dz}, \quad (2a)$$

$$\tau_y = -K_m \frac{dV}{dz}, \quad (2b)$$

$$H = -K_h \frac{d\Theta}{dz}, \quad (2c)$$

where K_m and K_h are the eddy diffusivities, assumed to be of the form

$$K_m = l^2 S f_m, \tag{3a}$$

$$K_h = l^2 S f_h, \tag{3b}$$

where l is the mixing length in neutral conditions, S is the wind shear, and f_m and f_h are empirical functions of the Richardson number, defined as follows,

$$f_m = \frac{1}{(1 + 300 Ri^2)^{3/2}}, \tag{4a}$$

$$f_h = \frac{1}{0.9(1 + 250 Ri^2)^{3/2}}. \tag{4b}$$

Above $Ri = N^2/S^2$ is the Richardson number, $N = (\beta\Gamma)^{1/2}$ is the Brunt–Väisälä frequency, $\beta = g/T_o$ is the buoyancy parameter, and $\Gamma = d\Theta/dz$ is the actual gradient of the potential temperature. The form of the above stability functions was obtained based on SHEBA observations in the surface layer (Sorbjan 2010; Sorbjan and Grachev 2010) for $Ri < 0.7$.

Equation 3a follows from an expressions for the eddy viscosity $K_m = l^2 S$ of Prandtl (1932), derived under the assumption that thermal stratification is neutral. The mixing length characterizes dominant eddies, and is formally defined as $l = \tau^{1/2}/S$, where $\tau = (\tau_x^2 + \tau_y^2)^{1/2}$. In close proximity of the underlying surface, observations show that $S = u_*/(\kappa z)$, where $u_* = \tau^{1/2}$ is the friction velocity, and $\kappa = 0.4$ is the von Karman constant. This implies that the mixing length in the neutral surface layer is a linear function of height $l = \kappa z$.

Farther from the surface, the growth of the mixing length with height is expected to be gentler (Sorbjan 2012a). This fact can be taken into consideration by adopting the inverse linear approximation of Delage (1974), between the limits of the mixing length near the underlying surface ($= \kappa z$) and in the neutral boundary layer ($= \lambda_o$): $1/l = 1/(\kappa z) + 1/(\lambda_o)$, which is equivalent to $l = z/(1 + \kappa z/\lambda_o)$. Blackadar (1962) suggested that $\lambda_o = 0.009 u_*/f$, where f is the Coriolis parameter. Following Huang et al. (2013), we employ an additional modification of the mixing length by proposing the inverse linear approximation of the form: $1/l = 1/(\kappa z) + 1/\lambda_m$, where $1/\lambda_m = 1/\lambda_o + 1/\lambda_B$, and λ_B is a stability parameter, which takes into consideration that the boundary layer is topped by the stably-stratified free atmosphere. This yields,

$$l = \frac{\kappa z}{1 + \frac{\kappa z}{\lambda_o}(1 + \lambda_o/\lambda_B)}. \tag{5}$$

Huang et al. (2013) concluded, based on a series of LES, that

$$\lambda_B = \lambda_s/Ri, \tag{6}$$

where $\lambda_s = 0.27$ m, and we will assume that $\lambda_s = 1$ m. Note that when, $\lambda_o/\lambda_B \rightarrow 0$ then $l \rightarrow \kappa z/(1 + \kappa z/\lambda_o)$.

The stability correction in Eq. 5 causes the mixing length l to be reduced in the upper portion of the SBL. For example, for $u_* \approx 0.3$ m s⁻¹, $f = 10^{-4}$ s⁻¹, and $Ri = 0.2$, we obtain $\lambda_o \approx 33$ m, $\lambda_B = \lambda_s/Ri = 5$ m, and $\lambda_o/(1 + \lambda_o/\lambda_B) \approx 4.3$ m. In addition, we will also assume that for $Ri > 0.7$ turbulence vanishes, and $l = 0$.

It should be noted that the turbulence parametrization Eqs. 2–6 is diagnostic, i.e. it is not directly dependent on time, and also that turbulence is characterized by the mean-state parameters in the entire range of eddies. Its intensity results from the local competition between the vertical wind shear and the stabilizing effects of the background buoyancy. The wind

shear S supplies the kinetic energy for turbulent motion, while buoyancy, expressed by the Brunt–Väisälä frequency N , acts to restrain it. If $S^2 > N^2$ (i.e. $Ri < 1$), shear production dominates and turbulence is amplified. Otherwise, buoyancy prevails and turbulence is suppressed. The system has one internal governing stability parameter, the Richardson number Ri , which dynamically adjusts to the boundary conditions, and to the external forcing. The profiles S^2 and N^2 are smooth, without fluctuations observed in the atmosphere (e.g. Sorbjan and Balsley 2008). Thus, the effect of turbulent mixing is assumed to be represented by the mixing length.

The semi-empirical formulation of the mixing length, Eqs. 5 and 6, has a shortcoming related to the fact that l is not local. The mixing length locally depends on the Richardson number Ri , but it is also a prescribed function of the height z . Such a deficiency can be improved by considering more advanced closure schemes. Sorbjan and Czerwinska (2013) found that Eqs. 5 and 6 do not work well in more complex cases, and that improvement can be achieved by assuming that $l \approx \sigma_w/N$, or $l \approx \beta\sigma_\theta/N^2$, where σ_w and σ_θ are the standard deviations of the vertical velocity and temperature.

2.2 Initial and Boundary Conditions

The system (1)–(6) is augmented by the no-slip boundary conditions at the surface, and the free-slip conditions at the top of the vertical domain,

$$\text{at } z = z_0 : U = 0, V = 0, \Theta = \Theta_0 - C_R t, \quad (7a)$$

$$\text{at } z = D : dU/dz = 0, dV/dz = 0, d\Theta/dz = \gamma, \quad (7b)$$

where z_0 is the aerodynamic roughness length, D is the vertical extent of the considered domain, Θ_0 is the initial surface temperature, γ is the value of the potential temperature gradient above the boundary layer, C_R is the cooling rate, and t is time.

The adopted initial condition formulation follows the GEWEX Atmospheric Boundary layer Study (GABLS) intercomparison set-up (Cuxart et al. 2006). It defines a neutrally stratified layer with a potential temperature $\Theta_0 = 265$ K, extending up to 100 m; above the 100 m layer, the potential temperature increases according to the gradient $\gamma = 0.01$ K m⁻¹. The vertical domain of the model is 2,910 m. The x -axis of the coordinate system is aligned with the geostrophic wind vector, such that $U_g = G$, $V_g = 0$, with the geostrophic wind G set to 8 m s⁻¹. The Coriolis parameter is $f = 1.39 \times 10^{-4}$ s⁻¹, which corresponds to latitude 73°N, and we take $z_0 = 0.1$ m. The initial flow is assumed geostrophic. In the basic set-up of the model, a prescribed surface cooling rate of $C_R = 0.25$ K h⁻¹ is applied for 9 or 24 h. In the other two runs, the cooling rate was applied for the first 8 h, followed by 1- or 2-h period of warming with $C_R = -0.25$ K h⁻¹. The external forcing s_u, s_v, s_θ is not considered herein.

It could be noted that, when $C_R = 0$ and $\gamma > 0$, the resulting boundary layer is stable. Turbulence generated by shear causes the upper part of the SBL to be cooled, and the lower part to be slightly warmed. For the pure neutral case to exist, it is required that $C_R = 0$ and $\gamma = 0$. When the cooling rate C_R increases, the depth of the SBL becomes smaller.

2.3 Numerical Solution

The model equations were solved numerically by using the method described in the Appendix. In order to obtain sufficient accuracy and to resolve the logarithmic sublayer, the grid spacing was very fine and non-uniform (logarithmic), with grid points located at $z_j = 10^{[\zeta_0 + (j-1)\delta z]}$ where $\zeta_0 = \log_{10}(z_0)$, δz is the grid increment, assumed to be equal to 0.018. The time

increment was also small, equal to 0.05 s. The number of grid points was typically 250, with the grid increment along the vertical coordinate changed from a fraction of z_0 near the surface, to about 120 m near the upper boundary. The unknown values U , V , and Θ were defined at levels z_j , and the eddy diffusivities K_m , K_h , temperature gradient Γ , shear S , and fluxes at midpoints $z_{j\pm 1/2}$.

The fine resolution ensures that the Monin–Obukhov similarity is exactly satisfied in the lower portion of the model domain. Consequently, the model does not require evaluation of the surface fluxes by inverting the Monin–Obukhov similarity expressions, as done in coarse-resolution SCMs. The surface fluxes can be directly obtained from Eqs. 2–5, by using gradients calculated for the first two grid points. A linear grid can also be used in the model for practical purposes, which requires applying the Monin–Obukhov similarity theory near the underlying surface in order to derive fluxes based on gradients. In this case, the number of grid points can be significantly smaller.

3 Results

3.1 Vertical Profiles

The vertical profiles of the potential temperature, wind speed, and turbulent fluxes, obtained from the 9-h basic run of our SCM, are shown in Fig. 1a–c. The results from high-resolution LES, performed at the University of Hannover, are also presented (Raash and Etling 1991; Raash and Schröter 2001). The LES and the SCM runs were performed for analogous initial conditions and forcing. The SCM results are presented as solid lines in the figure, and agree well with the LES results, which are represented by dashed red lines.

The potential temperature for the 9-h basic run is depicted in Fig. 1a together with the initial condition. Results of both models show the surface temperature of about 263 K, and similar profile curvatures in the boundary layer. The local wind maximum (low level jet) in Fig. 1b is about 9.5 m s^{-1} , and takes place at $z = 140 \text{ m}$. Both turbulent fluxes, $-H$ and τ , decrease with height (in Fig. 1c), and reach relatively small values at levels above 150 m. The results of the current version of the model (Fig. 1) are not significantly different from the previous version (Fig. 2 in Sorbjan 2012b). Nonetheless, the new formulation shows that the SCM very closely reproduces now the LES curves in Fig. 1.

The main difference between the SCM presented here and other SCMs, research and operational (e.g., Duynkerke 1991; Kim and Mahrt 1992; Galmarini et al. 1998; Beare and Mac Vean 2004; Edwards et al. 2006), is in the form of the stability functions f_m and f_h , and the adjustable values of λ_m (see Sect. 2.1). The values of λ_m , for the models included in the GABLS intercomparison, varied between 40 and 200 m. Generally, operational models utilize a pragmatic form of f_m and f_h , which slowly decay with Ri , and cause higher mixing efficiencies than would be expected based on local observations. As a consequence, such models avoid an excessive cooling near the surface over land points, which improves operational verification scores, but is not physically realistic.

Figure 2a depicts profiles of the Brunt–Väisälä frequency N (red line), shear S (blue line), and the Richardson number Ri (black line). Referring to the thermal stability classification of Sorbjan (2010), based on the values of the Richardson number, one can verify in the figure that:

- (i) the “near-neutral” regime ($0 < Ri < 0.02$) is located within the first 3 m above the ground,

Fig. 1 Model results obtained in the 9-h basic run: **a** the potential temperature, **b** the wind-velocity modulus, **c** the negative heat flux $-H$ and the modulus of the momentum flux τ . Profiles obtained in the University of Hannover LES simulations (Raash and Etling 1991; Raash and Schröter 2001) are indicated by red dashed lines

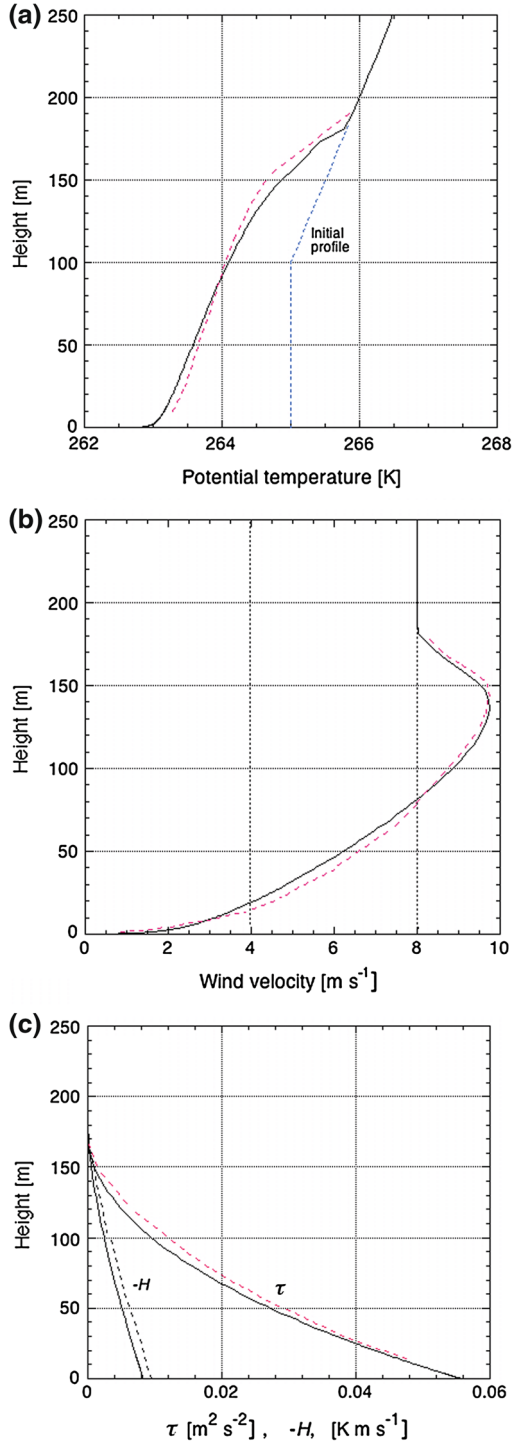
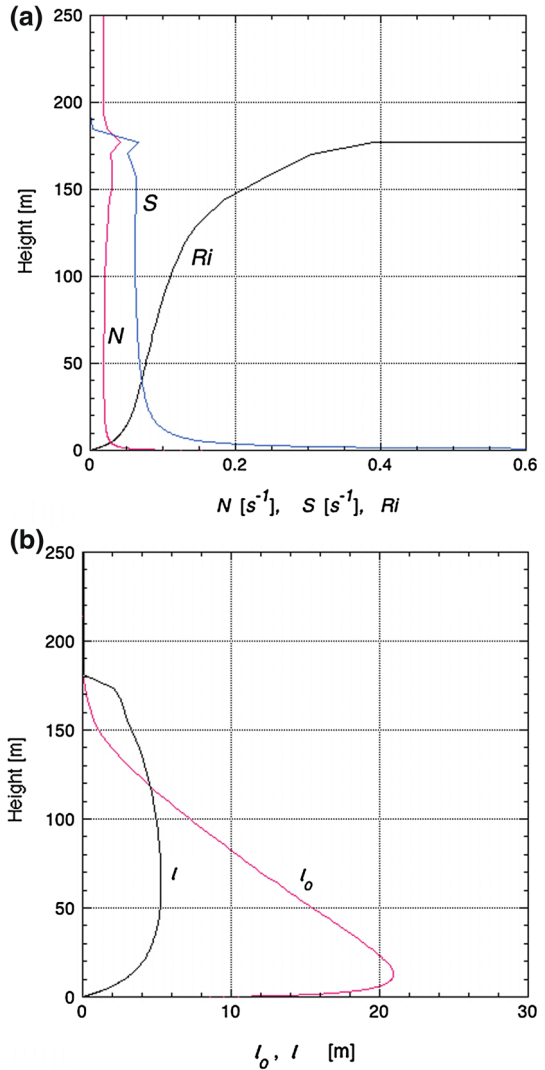


Fig. 2 Profiles of: **a** the Brunt–Väisälä frequency N , shear S , and the Richardson number Ri , **b** the mixing length l and the Ozmidov length $l_o = \varepsilon^{1/2}/N^{3/2}$, obtained in the 9-h basic run. The Ozmidov length l_o was estimated based on Eq. 13a



- (ii) the “stable” layer ($0.02 < Ri < 0.12$), extends from 3 m to about 108 m,
- (iii) the “very stable” layer ($0.12 < Ri < 0.7$), stretches from 108 to 180 m,
- (iv) the “extremely stable” layer ($Ri > 0.7$) is located above the level of 180 m.

Figures 1 and 2 indicate that, at the level $z = 180$ m, which can be considered as the height of the boundary layer, there is no cooling effect with respect to the assumed initial temperature, the wind velocity is geostrophic, and the turbulent fluxes are practically zero. The Brunt–Väisälä frequency has a local maximum, and the Richardson number Ri sharply increases with height. Figure 2b shows profiles of the mixing length l and the Ozmidov length $l_o = \varepsilon^{1/2}/N^{3/2}$, where the dissipation rate ε was evaluated based on Eq. 12a below. The Ozmidov length is the outer scale of isotropic turbulence in stable stratified flows. Within the first 10 m above the surface, the mixing length varies linearly, and above the surface

layer the increase of the mixing length is significantly reduced. At scales smaller than l_o , buoyancy has only a minor damping effect on isotropic turbulence, but dominates at larger ones. Consequently, based on Fig. 2b, we expect that below the level of 120 m, where $l_o < l$, turbulence is expected to be isotropic, and anisotropic above this level.

3.2 Universal Formulation Within the Model

Sorbjan (2010) introduced the following local scales for velocity, temperature, length:

$$U_N = l N, \tag{8a}$$

$$T_N = l \Gamma = l N^2 / \beta, \tag{8b}$$

$$L_N = l. \tag{8c}$$

The above scales involve the Brunt–Väisälä frequency N , and therefore will be referred to as the “gradient-based N -scales”. In terms of the above scales, the following expressions can be directly obtained based on (2)–(4),

$$\frac{\tau}{U_N} = \frac{f_m}{Ri} = \frac{1}{Ri(1 + 300Ri^2)^{3/2}}, \tag{9a}$$

$$\frac{H}{U_N T_N} = \frac{f_h}{Ri^{1/2}} = \frac{1}{0.9Ri^{1/2}(1 + 250Ri^2)^{3/2}}, \tag{9b}$$

$$Pr = \frac{K_m}{K_h} = \frac{f_m}{f_h} = \frac{Ri}{Rf} = 0.9 \frac{(1 + 250Ri^2)^{3/2}}{(1 + 300Ri^2)^{3/2}} \tag{9c}$$

where $Rf = -\beta H / (\tau S)$ is the flux Richardson number, and Pr is the Prandtl number. Note that Eq. 9c indicates that $Pr < 1$ (Sorbjan and Grachev 2010).

On the other hand, one can also obtain:

$$\Psi_m \equiv \frac{l_S}{U_*} = \frac{1}{f_m^{1/2}} = (1 + 300Ri^2)^{3/4}, \tag{10a}$$

$$\Psi_h \equiv \frac{l_\Gamma}{\Theta_*} = \frac{f_m^{1/2}}{f_h} = 0.9 \frac{(1 + 250Ri^2)^{3/2}}{(1 + 300Ri^2)^{3/4}}, \tag{10b}$$

$$\frac{l}{\Lambda_*} = \frac{\kappa}{Ri} \frac{f_m^{3/2}}{f_h} = \frac{\kappa}{0.9} \frac{Ri(1 + 300Ri^2)^{9/4}}{(1 + 250Ri^2)^{3/2}}, \tag{10c}$$

where the flux-based local scales are of the form:

$$U_* = \tau^{1/2}, \tag{11a}$$

$$\Theta_* = H / U_*, \tag{11b}$$

$$\Lambda_* = -\tau^{3/2} / (\kappa \beta H). \tag{11c}$$

Contrary to the Monin–Obukhov scales u_* , T_* , L_* , the above scales in Eq. 11 are height-dependent.

Because the turbulence parameterization is diagnostic, the expressions in Eqs. 9–10 are exactly satisfied within the model, for each moment of time, for each level in the SBL, for all any applied external forcing. Equations 10a–c extend the surface-layer (Monin–Obukhov) similarity formulation for the entire SBL. We note that the dimensionless expressions (9)–(10) are not independent of each other, and all are formulated in terms of two similarity functions f_m , f_h of the Richardson number Ri , defined by (4).

In the quasi-steady state, characteristics of turbulence do not significantly vary with time (see Fig. 6a). Consequently, budgets for the turbulent energy and for the temperature variance, can be approximately expressed in the following form,

$$K_m S^2(1 - Rf) = \varepsilon, \tag{12a}$$

$$\varepsilon_\theta = K_h \Gamma^2, \tag{12b}$$

where ε is the dissipation rate, and ε_θ is the dissipation for one-half of the temperature variance. Using Eqs. 3, 4, and 9, yields

$$\frac{\varepsilon}{U_N^2/t_s} = \frac{f_m}{Ri^3}(1 - Rf) = \frac{1}{Ri^3(1 + 300Ri^2)^{3/2}} \left[1 - \frac{Ri}{0.9} \frac{(1 + 300Ri^2)^{3/2}}{(1 + 250Ri^2)^{3/2}} \right], \tag{13a}$$

$$\frac{\varepsilon_\theta}{T_N^2/t_N} = \frac{f_h}{Ri^{1/2}} = \frac{1}{0.9Ri^{1/2}(1 + 250Ri^2)^{3/2}}. \tag{13b}$$

Since the dissipation rate ε is a positive-definite quantity, Eq. 13a allows us to conclude that the steady state, which results from a balance of shear production and buoyant-dissipative destruction, takes place only for $Rf < 1$. Equation 9c indicates that $Rf = 1$ when $Ri = Ri_s = 0.7$ (Sorbjan 2010). Thus, the steady-state turbulence would not be present at values of Ri exceeding $Ri_s = 0.7$, which is larger than the critical value $Ri_{cr} = 0.25$, implied by linear stability theory. In other words, at $Ri > Ri_s$, turbulence is expected to be non-stationary, i.e., decaying or sporadic. The inequality $Ri < Ri_{cr} = 0.25$ is a sufficient condition for the presence of steady-state turbulence, i.e., if satisfied, it guarantees that steady-state turbulence exists. The inequality $Ri < Ri_s = 0.7$ is a necessary condition for the presence of steady-state turbulence, i.e., it must be satisfied for steady-state turbulence to occur. Thus, the stability functions (4) for f_m and f_h are assumed valid for $Ri < 0.7$. Nonetheless, Grachev et al. (2013) argued that turbulence in the inertial range decays at $Ri > 0.25$.

The dimensionless similarity functions obtained at the end of the 9-h basic run are examined in Fig. 3 for the momentum flux $G_t = \tau/U_s$, heat flux $G_h = -H/(U_s T_s)$, wind shear $\Psi_m = l S/U_*$, temperature gradient $\Psi_h = l \Gamma/\Theta_*$, and for the ratio $l/(\kappa \Lambda_*)$ of the mixing length and the local Obukhov length. The lines in the figure indicate the numerical results, while the dots mark the values obtained from the analytical expression (9)–(10). As expected, the agreement is exact, i.e., the expressions (9)–(10) are exactly satisfied within the model for each moment of time, for each level in the SBL, and for all any external forcing applied in the model.

3.3 The Temperature-Flux Realizability Condition

Let us consider another gradient-based scaling system of the following form,

$$U_S = l S, \tag{14a}$$

$$T_S = l S^2/\beta, \tag{14b}$$

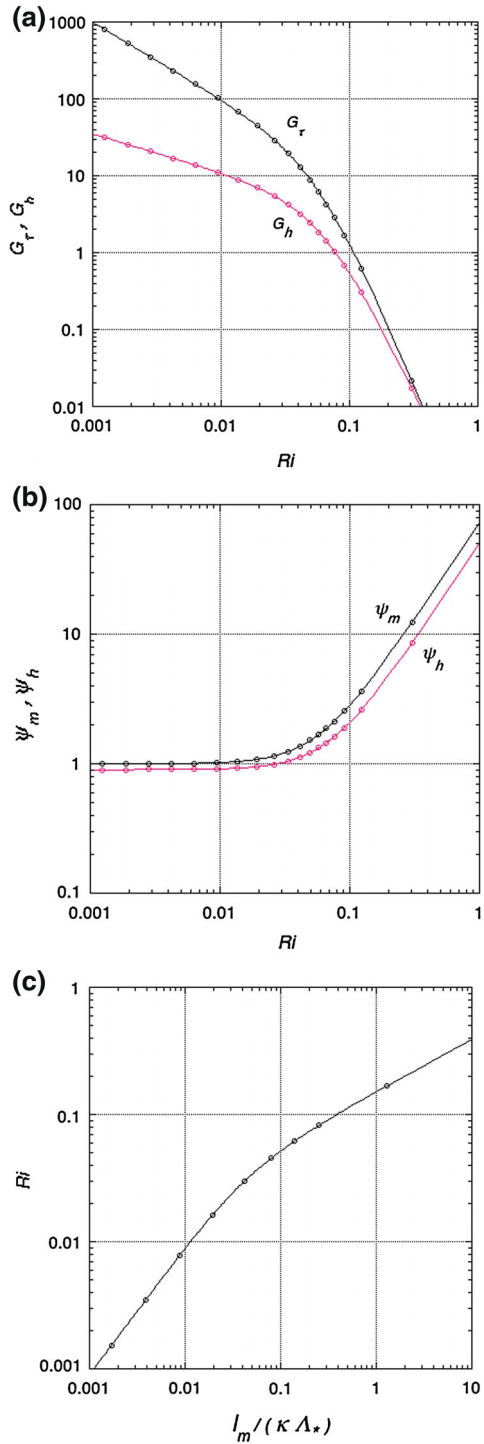
$$L_S = l. \tag{14c}$$

The above scales involve the shear S , and therefore will be referred to as the “gradient-based S -scales”. It can be readily verified that

$$U_S = U_N Ri^{-1/2}, \tag{15a}$$

$$T_S = T_N Ri^{-1}. \tag{15b}$$

Fig. 3 Dimensionless functions obtained in the 9-h basic run for: **a** momentum flux $G_t = \tau/U_s$ and heat flux $G_h = -H/(U_s T_s)$, **b** wind shear $\psi_m = l S/U_*$ and temperature gradient $\psi_h = l \Gamma/\Theta_*$, **c** the ratio of the mixed length and the local Obukhov length, l/Λ_* . Lines indicate the model results, while the *red dots* mark the values obtained from the analytical expression (9)–(10). The agreement of the numerical results and analytical values is exact



Consequently, the expressions (9b) can be rewritten as

$$-\frac{H}{U_S T_S} = Ri f_h = \frac{Ri}{0.9(1 + 250 Ri^2)^{3/2}}. \tag{16}$$

Figure 4 shows the dimensionless temperature flux $-H/(U_S T_S)$ obtained in the model as a function of Ri , and also as a function of height z . Figure 4a indicates that the dimensionless flux $-H/(U_S T_S)$ vanishes in neutral conditions at $Ri = 0$, and also in the very stable case, where Ri is large. It has a minimum where the first derivative with respect to Ri is zero. It can be readily verified based on Eq. 16 that the minimum, equal to $[0.9 \times 500^{1/2} (1.5)^{3/2}]^{-1} = -0.027$, is reached at $Ri_{\min} = (500)^{-1/2} = 0.0447$. Taking this result into consideration, we obtain

$$H_{\min}(z) = -0.027 U_S T_S = -0.027 \frac{l_m^2(z) S^3(z)}{\beta}, \tag{17}$$

which constitutes the realizability condition for the heat flux at a specific level z . The inequality $H(z) \geq H_{\min}(z)$ must be satisfied at any height z in the SBL. An expressions analogous to Eq. 17 was derived by Van de Wiel et al. (2011) based on Monin–Obukhov similarity theory in the surface layer; they found that the minimum of the temperature flux occurs at a larger value of $Ri_{\min} = 0.07$.

It can be noted that for $Ri_{\min} = 0.0447$, one obtains from Eq. 10c that $(l/\Lambda_*)_{\min} = 0.0311$, which implies that, in the surface layer where $l \approx \kappa z$, the parameter $(z/L_*)_{\min} = 0.0781$. The bin-averaged temperature flux, measured at five levels during the SHEBA experiment, show a similar minimum at z/L_* in the range $10^{-2} - 10^{-1}$ (A.A. Grachev, private communication, 2012).

In Fig. 4a, the values of the dimensionless heat flux $-H/(U_S T_S)$, obtained from the model, are plotted versus Ri ; the dots indicate the values plotted based on Eq. 16. The agreement of the numerical results (curves) and the analytical values described by Eq. 16 is exact. In Fig. 4b, the values of the dimensionless heat flux $-H/(U_S T_S)$ are plotted versus height; the minimum value of the dimensionless flux occurs at about $z = 11$ m. Figure 1c implies that, at $z = 11$ m, the heat flux $H = -0.0075$ K m s⁻¹; using Eq. 17, with $S = 0.1053$ s⁻¹ (see Fig. 2a), $l = 2.97$ m (see Fig. 2b), and $\beta = 0.0374$ m s⁻² K⁻¹, we obtain the same value.

In Fig. 4c, the actual heat flux H and the minimum permissible heat flux H_{\min} are plotted as functions of height. Values of both functions, H and H_{\min} , are equal at $z = 11$ m; below and above this level, the actual heat flux is larger that the permissible one. At the top of the SBL both values are equal to zero.

4 Temporal Evolution

Next, we discuss the temporal evolution of the nocturnal boundary layer, imposed by surface forcing, and also by the inertial effects. The inertial mechanism was first described by Blackadar (1957), as a phenomenon in the upper (nearly frictionless) part of the boundary layer. It involves undamped oscillations of wind vector around the geostrophic wind vector (Buajitti and Blackadar 1957). The phenomenon has a period of $T_i = 2\pi/f$, and is commonly observed in the atmosphere (e.g., Poulos et al. 2002). Inertial oscillations are considered as an important mechanism behind the occurrence of nocturnal low-level jets (e.g., Banta 2008).

Let us begin with a discussion of the nocturnal evolution of the boundary layer, provided by the model results. Figure 5 shows profiles of the potential temperature and the temperature flux, obtained in three model runs. In the first run, the underlying surface was cooled for 9 h

Fig. 4 Profiles of the temperature flux obtained in the basic run of the model: **a** the dimensionless temperature flux $-H/(U_S T_S)$ as a function of the Richardson number Ri (the dots indicate the values plotted based on Eq. 16—the agreement of the numerical results and analytical values is exact), **b** the dimensionless temperature flux $-H/(U_S T_S)$ as a function of height z , **c** the actual temperature flux H and the minimum flux H_{min} (see Eq. 17) as a function of height. Note that $H \geq H_{min}$, and that $H = H_{min}$ at $z = 11$ m, and at $z = 180$ m

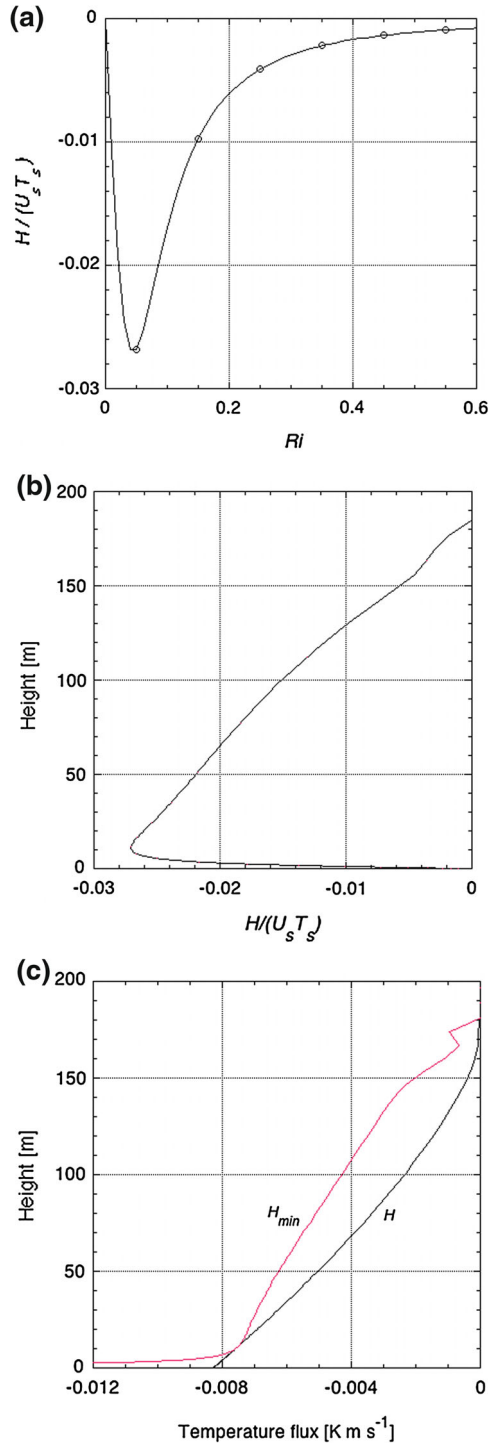
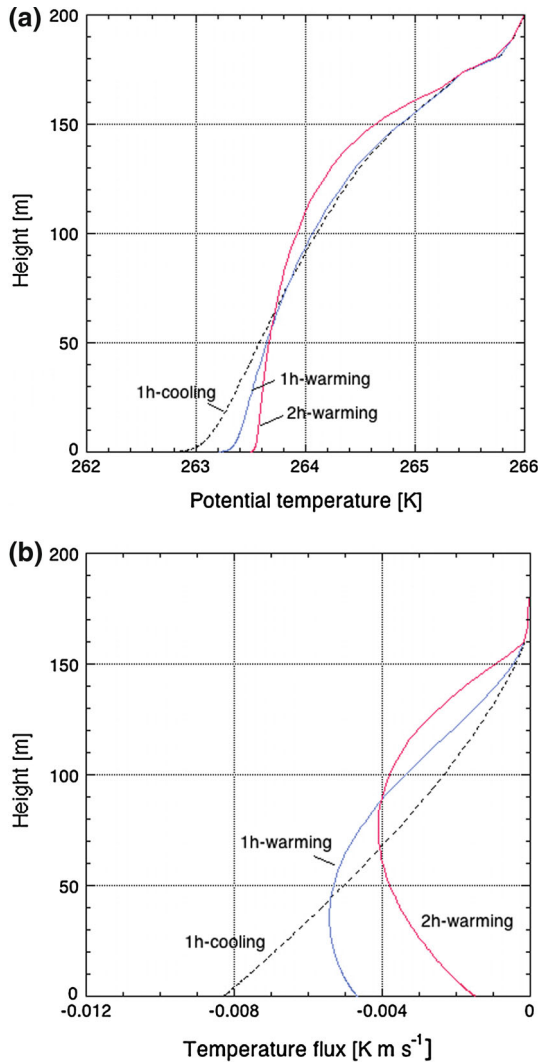


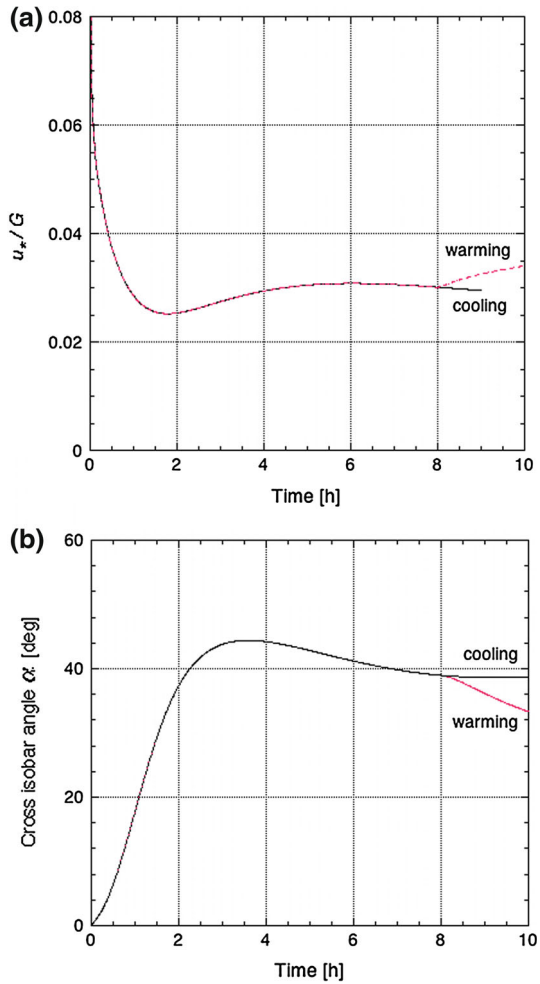
Fig. 5 Profiles of **a** the potential temperature, **b** the temperature flux, obtained after 8-h cooling with $C_R = 0.25 \text{ K h}^{-1}$, followed by: (i) additional 1-h cooling (*dotted lines*), (ii) 1-h warming with $C_R = -0.25 \text{ K h}^{-1}$ (*blue lines*), (iii) 2-h warming with $C_R = -0.25 \text{ K h}^{-1}$ (*red lines*)



at a rate $C_R = 0.25 \text{ K h}^{-1}$. In the second run, the 8-h cooling was followed by 1-h warming with the rate $C_R = -0.25 \text{ K h}^{-1}$. In the third run, the 8-h cooling was followed by 2-h warming with the same rate of $C_R = -0.25 \text{ K h}^{-1}$. The runs with warming intervals are intended to imitate the sunrise transition. The figure shows that when surface warming takes place, the temperature profiles are reshaped. They become more uniform with height, due to warming near the surface, while a strong temperature inversion layer forms at the top of the boundary layer. The heat flux, which is nearly linear in the cooling case, becomes strongly curved due to surface heating.

The corresponding time evolution of the drag coefficient u_*/G , and the cross-isobar angle α , is shown in Fig. 6. The figure indicates that frictional drag rapidly decreases with time (Fig. 6a), and decreased friction allows the Coriolis force to change the wind direction (Fig. 6b). After a few hours of cooling, a quasi equilibrium is achieved, with both para-

Fig. 6 The time evolution of: **a** the drag coefficient u_*/G , and **b** the cross-isobar angle α , obtained after 8-h cooling with $C_R = 0.25 \text{ K h}^{-1}$, followed by: (i) additional 2-h of cooling (black lines), (ii) 2-h warming with $C_R = -0.25 \text{ K h}^{-1}$ (red lines)

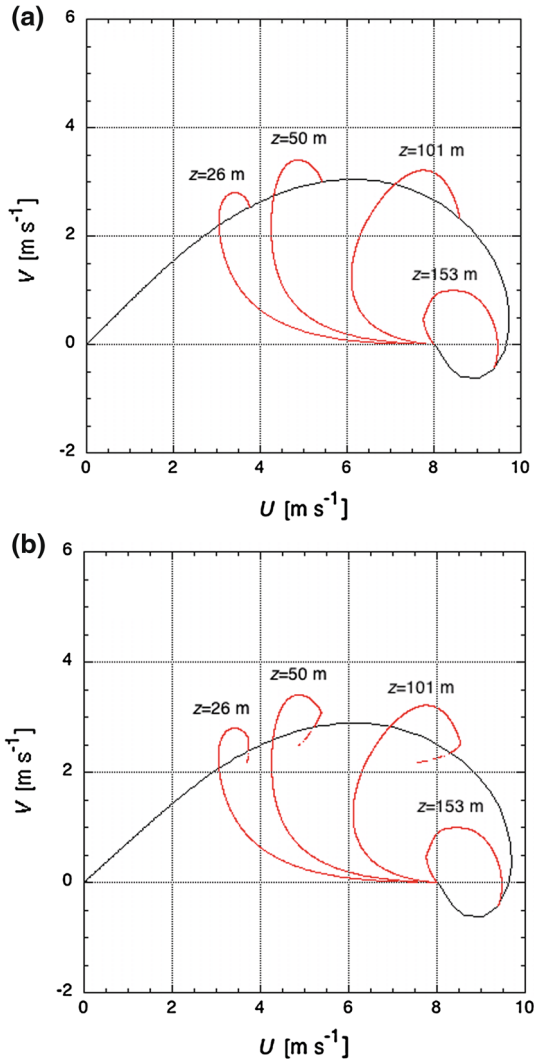


meters, u_*/G and α nearly constant with time. When the quasi-steady state is interrupted by the “sunrise” warming, the drag coefficient increases rapidly, and the cross-isobar angle decreases.

In Fig. 7, two “fixed-time” hodographs are presented as black lines. The first hodograph (Fig. 7a) was obtained after 9-h surface cooling of the boundary layer with the rate $C_R = 0.25 \text{ K h}^{-1}$. The second hodograph (Fig. 7b) is a result 8-h cooling with the rate C_R , followed by 1-h warming with the rate $C_R = -0.25 \text{ K h}^{-1}$. The red lines (“fixed-elevation” hodographs) indicate how the tips of the wind vectors evolve in time at four levels: $z = 26, 50, 101, \text{ and } 153 \text{ m}$. It should be remembered that the initial wind is geostrophic, of magnitude 8 m s^{-1} , and directed along the x -axis. This is an idealization within the model, since a non-zero crosswind is usually observed during late afternoon in the atmospheric boundary layer, resulting in a cross-isobar angle of about 5° . The effect of the initial condition is strong during the first part of the simulation.

In Fig. 7a, b, the angle between the actual wind at a given level (marked by a red point on the fixed-elevation hodograph) and the geostrophic wind increases with time within the

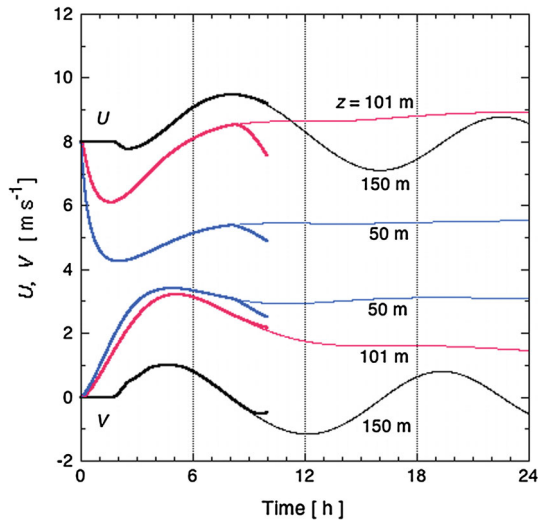
Fig. 7 Hodographs of the wind vector (*black lines*) obtained after: **a** 9-h surface cooling of the boundary layer with $C_R = 0.25 \text{ K h}^{-1}$, **b** 8-h cooling with $C_R = 0.25 \text{ K h}^{-1}$, followed by 1-h warming with $C_R = -0.25 \text{ K h}^{-1}$. The initial wind is geostrophic with $G = 8 \text{ m s}^{-1}$, located along the x -axis. The *red lines* (the fixed-elevation hodographs) indicate the endings of the wind vectors at the levels: 26, 50, 101 m, and 153 m. The *dashed lines in the right plot* are obtained during an additional 1-h warming (i.e., after 8-h cooling and 2-h warming) with $C_R = -0.25 \text{ K h}^{-1}$



first few hours of the boundary-layer development, and subsequently it slightly decreases (which is consistent with Fig. 6b). As a result, the red-line hodographs turn clockwise and take on the characteristic “horseshoe” shapes. Similar hodographs were presented in [Weng and Taylor \(2006\)](#).

The continuous segments of the red lines in Fig. 7a were obtained at $z = 26, 50,$ and 101 m , during the 9-h cooling. It should be noted that they will not change significantly even during a 24-h simulation (see the discussion below), because the quasi-steady state is reached after about 9 h. As a result, velocity components U and V are nearly constant with time; consequently the “horseshoe” hodographs in Fig. 7a will not become rounder. The continuous segments of the red lines in Fig. 7b were obtained at the same levels of $z = 26, 50,$ and 101 m , during the 8-h cooling and 1-h warming. The dotted segments mark the additional 1-h warming at the end of the simulation. The “warming” segments are nearly perpendicular

Fig. 8 Components of wind vectors at $z = 50, 101,$ and 150 m, obtained in two runs of the model: (i) during 24-h cooling with $C_R = 0.25 \text{ K h}^{-1}$ (thin lines), and (ii) 8-h cooling with $C_R = 0.25 \text{ K h}^{-1}$, followed by 2-h warming with $C_R = -0.25 \text{ K h}^{-1}$ (thick lines). The inertial period in both cases is $T_i = 12.55$ h. Within the first 8 h, the results of both runs coincide



to the continuous ones, which causes the red hodographs to appear more circular. At $z = 153$ m, the wind speed exceeds the value of the geostrophic wind, a phenomenon referred to as the low-level jet.

To further examine the transitory issues, let us consider Fig. 8, which shows the temporal evolution of wind-vector components U and V at three levels: $z = 50$ m (blue lines), 101 m (red lines), and 150 m (black lines). They were obtained in two model runs. The first run consisted of a 24-h cooling with $C_R = 0.25 \text{ K h}^{-1}$; the results are represented by thin lines. The second run included 8-h cooling with $C_R = 0.25 \text{ K h}^{-1}$, followed by 2-h warming with $C_R = -0.25 \text{ K h}^{-1}$. The results are marked by thick lines. The second run was terminated at the instant that the surface heat flux reached values near zero (as the turbulence closure applies only to cases when $Ri > 0$). Within the first 8 h the results of both runs coincide.

At $z = 150$ m, near the top of the boundary layer, inertial oscillations of both components of wind velocity develop with a period of about 13 h (note that for the value $f = 1.39 \times 10^{-4} \text{ s}^{-1}$, adopted in our model, the inertial period is $T_i = 12.55$ h). The oscillations are damped by turbulent mixing, as the second maximum ($\approx 8.8 \text{ m s}^{-1}$) at $t \approx 22$ h is noticeably lower than the first maximum ($\approx 9.5 \text{ m s}^{-1}$) at $t \approx 8$ h. The oscillations at the top of the boundary layer (at $z = 180$ m) are not damped (not shown). Within the boundary layer ($z = 50$ and 101 m), the internal oscillations are entirely damped after about 9 h, and the velocity components reach “quasi-equilibrium”.

In the case of the 8-h cooling followed by 2-h warming, the quasi-steady state within the boundary layer is not reached. The U -component at $z = 50$ and 101 m begins to decrease from the moment that warming begins (such effects on the V -component are also noticeable but less pronounced). As a result, the three lines, representing the U -component at $z = 50, 101,$ and 150 m during the first 10 h of the simulation are similar in Fig. 8, i.e., are nearly parallel, and have a shape of a sine function with a period of about 10 h. This value is less than the inertial period of $T_i = 12.55$ h, and consequently, these sine-like functions cannot be classified as inertial oscillations.

The above discussion implies that the development of “horse-shoe” shaped, “fixed-elevation” hodographs in the interior of the nocturnal boundary layer (in Fig. 7) are only partly caused by the damped inertial effects (as in the model of Van de Wiel et al. 2010),

and are strongly affected by surface forcing due to the sunrise warming. The pure inertial oscillations occur only near the top of the SBL, as predicted by Blackadar’s (1957) theory.

5 Conclusions

Our primary purpose was to examine properties of a single-column model of the SBL, specifically the consistency of turbulence parametrization, self-similar properties, and the effects of applied forcing.

The turbulence closure of the model is diagnostic. It employs the K-theory approach, with semi-empirical formulation of the mixing length, which locally depends on the Richardson number Ri , but is also dependent on height. The empirical stability functions of Ri are evaluated based on the SHEBA data. The model has one internal, governing stability parameter, Ri , which dynamically adjusts to the boundary conditions and to the external forcing. A comparison of the model results with the high-resolution, large-eddy simulations performed at the University of Hannover, reflects very good agreement for the considered GABLS case.

When expressed in terms of similarity scales, the model results are universal, i.e. they are satisfied in the entire SBL, for all time, and for the considered external forcing. Specifically, Eqs. 10a and 10b extend the surface-layer (Monin–Obukhov) similarity formulation for gradients to the entire SBL. The expressions (9)–(10), (13) for fluxes, gradients, and dissipation rates, are formulated in terms of two empirical functions f_m, f_h of Ri .

Employing the gradient-based S -scales U_S, T_S allows identification of the minimum of the dimensionless heat flux, with $H/(U_S T_S = -0.027$, reached at $Ri = 0.0447$. The minimum defines the realizability limit for the heat flux in the SBL, which cannot be locally smaller than the value $H_{\min}(z) = -0.027 l_m^2(z) S^3(z)/\beta$. The numerical experiments show that the development of “horse-shoe” shaped, fixed-elevation wind hodographs in the interior of the SBL around sunrise is controlled by surface thermal forcing, rather than by inertial effects.

Acknowledgments This work has been supported by the National Science Foundation Physical and Dynamic Meteorology Program under Grant ATM-0938293, and by the Polish National Science Centre Grant 0572/B/P01/2011/40.

Open Access This article is distributed under the terms of the Creative Commons Attribution License which permits any use, distribution, and reproduction in any medium, provided the original author(s) and the source are credited.

Appendix: A Computational Scheme

In order to solve the system (1)–(7), a non-linear vertical mesh was introduced. The unknown values U, V, Θ were defined at levels z_j , and the eddy diffusivity at midpoints $z_{j\pm 1/2}$. This led to the following system of equations for temperature,

$$\frac{\Theta_j^{k+1} - \Theta_j^k}{\Delta t} = \frac{K_{j+1/2} \left(\frac{\Theta_{j+1}^{k+1} - \Theta_j^{k+1}}{z_{j+1} - z_j} \right) - K_{j-1/2} \left(\frac{\Theta_j^{k+1} - \Theta_{j-1}^{k+1}}{z_j - z_{j-1}} \right)}{(z_{j+1/2} - z_{j-1/2})} + s_j^{k+1}, \tag{18}$$

where $t = t^k = k\Delta t, j = 2, \dots, n, k = 1, \dots, m, \Delta t$ is the time increment, and $\Theta(z, t) = \Theta(z_j, t^k) = \Theta_j^k$.

To solve the above system of linear equations, the sweeping method was used at each timestep. For this purpose, Eq. 18 was rewritten in the following form,

$$A_j X_{j+1} - B_j X_j + C_j X_{j-1} = -F_j, \tag{19}$$

where for $j = 2, \dots, n - 1$, $X_j = \Theta_j^{k+1}$, and A_j, B_j, C_j and F_j were coefficients defined as

$$A_j = \frac{\Delta t K_{j+1/2}}{(z_{j+1} - z_j)(z_{j+1/2} - z_{j-1/2})}, \tag{20a}$$

$$B_j = 1 + A_j + C_j, \tag{20b}$$

$$C_j = \frac{\Delta t K_{j-1/2}}{(z_j - z_{j-1})(z_{j+1/2} - z_{j-1/2})}, \tag{20c}$$

$$F_j = \Theta_j^k + s_j^{k+1}. \tag{20d}$$

The boundary conditions were expressed in a general form, which is consistent with Eq. 19, viz.

$$A_1 X_2 + B_1 X_1 = F_1 \quad \text{for } i = 1, \tag{21a}$$

$$B_n X_n + C_n X_{n-1} = F_n \quad \text{for } i = n. \tag{21b}$$

The solution of the system of $n+1$ equations (18) and (21) was assumed to be in the form

$$X_{j-1} = a_j X_j + b_j, \tag{22}$$

where for $i = n, \dots, 2$, a_j and b_j are coefficients.

Note that substituting (21) into (19), yields,

$$X_j = \frac{A_j}{(B_j - C_j a_j)} X_{j+1} + \frac{(F_j + C_j b_j)}{(B_j - C_j a_j)}. \tag{23}$$

The above result implies that

$$a_{j+1} = \frac{A_j}{(B_j - C_j a_j)}, \tag{24a}$$

$$b_{j+1} = \frac{(F_j + C_j b_j)}{(B_j - C_j a_j)}, \tag{24b}$$

for $i = 2, \dots, n - 1$. From the boundary conditions, we obtained

$$a_2 = -\frac{A_1}{B_1}, \tag{25a}$$

$$b_2 = \frac{F_1}{B_1}, \tag{25b}$$

and

$$X_n = \frac{(F_n - C_n b_n)}{(B_n + C_n a_n)}. \tag{26}$$

The solution can be found in two ‘‘sweeps’’. First, coefficients a_j and b_j are found from Eqs. 25, 24, for $j = 2, \dots, n$. In the second sweep, X_n can be calculated from Eq. 26, and the solution X_{j-1} is obtained from Eq. 22.

The momentum equations were solved by using the matrix version of the sweeping method. For the following approximation

$$\frac{U_j^{k+1} - U_j^k}{\Delta t} = \frac{K_{j+1/2} \left(\frac{U_{j+1}^{k+1} - U_j^{k+1}}{z_{j+1} - z_j} \right) - K_{j-1/2} \left(\frac{U_j^{k+1} - U_{j-1}^{k+1}}{z_j - z_{j-1}} \right)}{(z_{j+1/2} - z_{j-1/2})} + f(V_j^{k+1} - V_g) + s_u, \tag{27a}$$

$$\frac{V_j^{k+1} - V_j^k}{\Delta t} = \frac{K_{j+1/2} \left(\frac{V_{j+1}^{k+1} - V_j^{k+1}}{z_{j+1} - z_j} \right) - K_{j-1/2} \left(\frac{V_j^{k+1} - V_{j-1}^{k+1}}{z_j - z_{j-1}} \right)}{(z_{j+1/2} - z_{j-1/2})} - f(U_j^{k+1} - U_g) + s_v, \tag{27b}$$

the system (27) can be rewritten in the form

$$A_j U_{j+1}^{k+1} - (B_j U_j^{k+1} - E_j V_j^{k+1}) + C_j U_{j-1}^{k+1} = -U_j^k + \Delta t f V_g - s_u, \tag{28a}$$

$$A_j V_{j+1}^{k+1} - (B_j V_j^{k+1} + E_j U_j^{k+1}) + C_j V_{j-1}^{k+1} = -V_j^k - \Delta t f V_g - s_v, \tag{28b}$$

where coefficients A_j , B_j , and C_j are defined by Eq. 20, and

$$E_j = f \Delta t. \tag{29}$$

The above system is equivalent to the matrix equation

$$\underline{A}_j \underline{W}_{j+1} - \underline{B}_j \underline{W}_j + \underline{C}_j \underline{W}_{j-1} = -\underline{F}_j \tag{30}$$

where:

$$\underline{A}_j = \begin{bmatrix} A_j & 0 \\ 0 & A_j \end{bmatrix}, \quad \underline{B}_j = \begin{bmatrix} B_j & -E_j \\ E_j & B_j \end{bmatrix}, \quad \underline{C}_j = \begin{bmatrix} C_j & 0 \\ 0 & C_j \end{bmatrix},$$

$$\underline{F}_j = \begin{bmatrix} U_j^k - f \Delta t V_g + s_u \\ V_j^k + f \Delta t U_g + s_v \end{bmatrix}, \quad \underline{W}_j = \begin{bmatrix} U_j^{k+1} \\ V_j^{k+1} \end{bmatrix}$$

and $j = 2, \dots, n - 1$.

The boundary conditions can be expressed in the general form, which is consistent with Eq. 30

$$\underline{A}_1 \underline{W}_2 + \underline{B}_1 \underline{W}_1 = \underline{F}_1 \quad \text{for } i = 1, \tag{31a}$$

$$\underline{B}_n \underline{W}_n + \underline{C}_n \underline{W}_{n-1} = \underline{F}_n \quad \text{for } i = n. \tag{31b}$$

The solution of Eq. 28 is assumed to have the following form:

$$\underline{W}_{j-1} = \underline{a}_j \underline{W}_j + \underline{b}_j, \tag{32}$$

where \underline{a}_j and \underline{b}_j are matrices 2×2 , and $j = n, \dots, 2$.

Substituting Eq. 32 into Eq. 30, yields:

$$\underline{a}_{j+1} = (\underline{B}_j - \underline{C}_j \underline{a}_j)^{-1} \underline{A}_j, \tag{33a}$$

$$\underline{b}_{j+1} = (\underline{B}_j - \underline{C}_j \underline{a}_j)^{-1} (\underline{F}_j + \underline{C}_j \underline{b}_j), \tag{33b}$$

where $i = 2 \dots n - 1$. From the boundary conditions we obtain

$$\underline{a}_2 = -\underline{B}_1^{-1} \underline{A}_1, \tag{34a}$$

$$\underline{b}_2 = \underline{B}_1^{-1} \underline{F}_1, \tag{34b}$$

and

$$\underline{W}_n = (\underline{B}_n + \underline{C}_n \underline{a}_n)^{-1} (\underline{E}_n - \underline{C}_n \underline{b}_n). \quad (35)$$

Specifically, when $A_1 = 0$, $B_1 = E$, $F_1 = 0$, $B_n = E$, $C_n = -E$ (where E is an identity matrix), then $\underline{a}_2 = 0$, $\underline{b}_2 = 0$, and $\underline{W}_n = (E - \underline{a}_n)^{-1} (\underline{E}_n + \underline{b}_n)$.

In order to find a solution, the matrices \underline{a}_j and \underline{b}_j were found from Eqs. 33 and 34 within the first “sweep”. Then, the solution was obtained in the second “sweep” from Eqs. 35 and 32.

References

- Andreas EL, Fairall CW, Guest PS, Persson POG (1999) An overview of the SHEBA atmospheric surface flux program. In: 13th Symposium on boundary layers and turbulence. American Meteorological Society proceedings, Dallas, TX, pp 550–555
- Banta RM (2008) Stable-boundary-layer regimes from the perspective of the low-level jet. *Acta Geophys* 56(1):58–87
- Beare RJ, Mac Vean M (2004) Resolution sensitivity and scaling of large-eddy simulations of stable boundary layer. *Boundary-Layer Meteorol* 112:257–281
- Beare RJ, Mac Vean MK, Holtslag AA, Cuxart J, Esau I, Golaz J-C, Jimenes MA, Khairoutdinov M, Kosovic B, Lewellen D et al (2006) An intercomparison of large eddy-simulations of the stable boundary layer. *Boundary-Layer Meteorol* 118(2):247–272
- Blackadar AK (1957) Boundary layer wind maxima and their significance for the growth of nocturnal inversions. *Bull Am Meteorol Soc* 38:283–290
- Blackadar AK (1962) The vertical distribution of wind and turbulent exchange in neutral atmosphere. *J Geophys Res* 67:3095–3103
- Blumen W, Banta RM, Burns SP, Fritts DC, Newsom R, Poulos GS, Sun J (2001) Turbulence statistics of a Kelvin–Helmholtz billow event observed in the night-time boundary layer during the Cooperative Atmosphere–Surface Exchange Study field program. *Dyn Atmos Oceans* 34:189–204
- Buajitti K, Blackadar AK (1957) Theoretical studies of diurnal wind-structure variations in the planetary boundary layer. *Q J R Meteorol Soc* 83(358):486–500
- Cuxart J, Yagüe C, Morales G, Terradellas E, Orbe J, Calvo J, Fernandez A, Soler MR, Infante C, Buenestado P, Espinalt A, Joergensen HE, Rees JM, Vila J, Redondo JM, Cantalapedra IR, Conangla L (2000) Stable atmospheric boundary layer experiment in Spain (SABLES, 98). A report. *Boundary-Layer Meteorol* 96:337–370
- Cuxart J, Holtslag AAM, Beare RJ, Bazile E, Beljaars A, Cheng A, Conangla L, Ek M, Freeman F, Hamdi R et al (2006) Single column model intercomparison for a stably stratified atmospheric boundary layer. *Boundary-Layer Meteorol* 118(2):273–303
- Delage Y (1974) A numerical study of the nocturnal atmospheric boundary layer. *Q J R Meteorol Soc* 100:351–364
- Derbyshire SH, Wood N (1994) The sensitivity of stable boundary layers to small slopes and other influences. In: Rockliff N, Castro IP (eds) *Proceedings of the 4th IMA conference waves and stably-stratified turbulence*. Clarendon Press, Oxford, pp 105–118
- Duynkerke PG (1991) Radiation fog: a comparison of model simulation with detailed observations. *Mon Weather Rev* 119(2):324–341
- Duynkerke PG (1999) Turbulence, radiation and fog in Dutch stable boundary layers. *Boundary-Layer Meteorol* 90:447–477
- Edwards JM, Beare RJ, Lapworth AJ (2006) Simulations of the observed evening transition and nocturnal boundary layers: single-column modelling. *Q J R Meteorol Soc* 132:61–80
- Galmarini S, Beets C, Duynkerke PG (1998) Stable nocturnal boundary layers: a comparison of one dimensional and large-eddy simulation models. *Boundary-Layer Meteorol* 88:181–210
- Grachev AA, Fairall CW, Persson POG, Andreas EL, Guest PS (2005) Stable boundary-layer scaling regimes: the SHEBA data. *Boundary-Layer Meteorol* 116(2):201–235
- Grachev AA, Andreas EL, Fairall CW, Guest PS, Persson OG (2013) The critical Richardson number and limits of applicability of local similarity theory in the stable boundary layer. *Boundary-Layer Meteorol* 147(1):51–82
- Ha K-J, Mahrt L (2003) Radiative and turbulent fluxes in the nocturnal boundary layer. *Tellus* 55A:317–327

- Huang J, Bou-Zeid E, Golaz JC (2013) Turbulence and vertical fluxes in the stable atmospheric boundary layer. Part II: A novel mixing-length model. *J Atmos Sci* 70:1528–1542
- Kim J, Mahrt L (1992) Simple formulation of turbulent mixing in the stable free atmosphere and nocturnal boundary layer. *Tellus* 44A:381–394
- Kosovic B, Curry JA (2000) A large-eddy simulations of a quasi-steady stratified atmospheric boundary layer. *J Atmos Sci* 57:1052–1068
- Kustas W, Li F, Jackson J, Prueger J, MacPherson J, Wolde M (2004) Effects of remote sensing pixel resolution on modeled energy flux variability of croplands in Iowa. *Remote Sens Environ* 92:535–547
- Mahrt L, Vickers D, Nakamura R, Soler MR, Sun J, Burns S, Lenschow DH (2001) Shallow drainage flows. *Boundary-Layer Meteorol* 101:243–260
- Mirocha JD, Kosovich B (2010) A large-eddy simulation study of the influence of subsidence on the stably stratified atmospheric boundary layer. *Boundary-Layer Meteorol* 134:1–21
- Monti P, Fernando HJS, Princevac M, Chan WC, Kowalewski TA, Pardyjak ER (2002) Observations of flow and turbulence in the nocturnal boundary layer over a slope. *J Atmos Sci* 59(17):2513–2534
- Nappo CJ (1991) Sporadic breakdown of stability in the PBL over simple and complex terrain. *Boundary-Layer Meteorol* 54:9–87
- Oncley SP, Foken T, Vogt R, Kohsiek W, de Bruin H, Bernhofer C, Christen A, van Gorsel E, Grantz D, Lehner I, Liebethal C, Liu H, Mauder M, Pitacco A, Ribeiro L, Weidinger T (2007) The energy balance experiment EBEX-2007. Part I: Overview and energy balance. *Boundary-Layer Meteorol* 123:1–28
- Persson POG, Fairall CW, Andreas EL, Guest PS, Perovich DK (2002) Measurements near the Atmospheric Surface Flux Group tower at SHEBA: near-surface conditions and surface energy budget. *J Geophys Res* 107(C10):8045, 21-1–21-35
- Poulos GS, Blumen W, Fritts DC, Lundquist JK, Sun J, Burns SP, Nappo C, Banta R, Newsom R, Cuxart J, Terradellas E, Balsley BB, Jensen ML (2002) CASES-99: a comprehensive investigation of the stable nocturnal boundary layer. *Bull Am Meteorol Soc* 83:555–581
- Prandtl L (1932) *Meteorologische Anwendungen der Stromungslehre*. *Beitr Phys Atmos* 19:188–202
- Raash S, Etling D (1991) Numerical simulations of rotating turbulent thermal convection. *Beitr Phys Atmos* 64:185–199
- Raash S, Schröter M (2001) PALM—a large-eddy simulation model performing on massively parallel computers. *Meteor Z* 10:363–372
- Sanz Rodrigo J, Anderson PS (2013) Investigation of the stable atmospheric boundary layer at Halley Antarctica. *Boundary-Layer Meteorol* 148(3):517–539
- Schwarz P, Law B, Williams M, Irvine J, Kurpius M, Moore D (2004) Climatic versus biotic constraints on carbon and water fluxes in seasonally drought-affected ponderosa pine ecosystems. *Glob Biochem Cycles* 18:1029–1037
- Shapiro A, Fedorovich E (2009) Katabatic flow induced by a cross-slope band of surface cooling. *Acta Geophys* 57:923–949
- Sorbjan Z (2010) Scaling and similarity laws in the stable boundary layer. *Q J R Meteorol Soc* 136:1243–1254
- Sorbjan Z (2012a) The height correction of the gradient-based and flux-based similarity functions in the stable boundary layer. *Boundary-Layer Meteorol* 142(1):21–31
- Sorbjan Z (2012b) A study of the stable boundary layer based on a single-column K-theory model. *Boundary-Layer Meteorol* 142(1):33–53
- Sorbjan Z, Balsley BB (2008) Microstructure of turbulence in the nocturnal boundary layer. *Boundary-Layer Meteorol* 129:191–210
- Sorbjan Z, Czerwinska A (2013) Statistics of turbulence in the stable boundary layer affected by gravity waves. *Boundary-Layer Meteorol* 148(1):73–91
- Sorbjan Z, Grachev AA (2010) An evaluation of the flux–gradient relationship in the stable boundary layer. *Boundary-Layer Meteorol* 135(3):385–405
- Stoll R, Porté-Agel F (2008) Large-eddy simulation of the stable atmospheric boundary layer using dynamic models with different averaging schemes. *Boundary-Layer Meteorol* 126(1):1–28
- Sun J, Burns S, Delany AC, Oncley T, Horst A, Lenschow D (2003) Heat balance in nocturnal boundary layer during CASES-99. *J Appl Meteorol* 42:1649–1666
- Sun J, Lenschow D, Burns S, Banta RM, Newsom RK, Coulter R, Frasier S, Ince T, Nappo C, Malsley BB, Jensen M, Mahrt L, Miller D, Skelly B (2004) Atmospheric disturbances that generate intermittent turbulence in nocturnal boundary layers. *Boundary-Layer Meteorol* 110:255–279
- Sun X, Weng W, Taylor PA (2006) An evaluation of several turbulence closure schemes for modelling thermally induced slope flows (12A.4). In: 17th AMS symposium on boundary layers and turbulence, San Diego, CA, USA

- Thomas C, Martin JG, Goeckede M, Siqueira MBS, Foken T, Law BE, Loescher HW, Katul G (2008) Estimating daytime subcanopy respiration from conditional sampling methods applied to multi-scalar high frequency turbulence time series. *Agric For Meteorol* 148:1210–1229
- Van de Wiel BJH, Moene AF, Steeneveld GJ, Baas P, Bosveld FC, Holtslag AAM (2010) A conceptual view on inertial oscillations and nocturnal low-level jets. *J Atmos Sci* 67:2679–2689
- Van de Wiel BJH, Basu S, Moene AF, Jonker HJJ, Steeneveld GJ, Holtslag AAM (2011) Comments on “An extremum solution of the Monin–Obukhov similarity equations”. *J Atmos Sci* 68:1405–1408
- Weng W, Taylor PA (2006) Modelling the one-dimensional stable boundary layer with an E-1 turbulence closure scheme. *Boundary-Layer Meteorol* 118:305–323